Impact of horizontal resolution on the regional climate simulations of the summer 1998 extreme rainfall along the Yangtze River Basin

Hongbo Liu,[1] Da-Lin Zhang,[2] and Bin Wang[1]

[1] In this study, the effects of varying horizontal grid resolutions on the regional climate model (RCM) simulation of the summer 1998 extreme rainfall events along the middle to lower reaches of the Yangtze-River Basin (YRB-ML) are examined using the Pennsylvania State University-National Center for Atmospheric Research mesoscale model (i.e., MM5). Results show that the MM5 simulation with the finest grid size of 4 km reproduces reasonably well the rainfall intensity and rainbelt distribution over the YRB-ML during all the Meiyu phases, whereas lower-resolution simulations tend to shift the east-west-oriented major rainbelt southwestward as a result of the generated local storms and excessive rainfall during the second Meiyu rainy phase in which vertical (horizontal) wind shears are weak (strong). The excessive rainfall occurs during the evening hours when the low-level jet is relatively strong and in the Meiyu frontal zone where convergence of warm and moist air is pronounced. Results reveal the importance of incorporating convective parameterizations in removing potential instability in heavy rain-producing storms even for RCMs with 3–5 km horizontal resolutions. It is highly desirable to use higher-resolution models with realistic parameterized and grid-scale cloud physics schemes to study the regional climate of heavy rainfall events.

1. Introduction

[2] Rapid growth of computing power has now allowed us to increase the horizontal and vertical resolutions of numerical models to better represent the orographical complexity, land-cover details, and small-scale precipitation processes. For example, today's general circulation models (GCMs) can be run at a grid size of 20 km to simulate the genesis and evolution of tropical cyclones [*Kang*, 2007] and the 20-year East Asian summer monsoon climate [*Kitoh and Kusunoki*, 2008], while real-data numerical weather prediction (NWP) models can be run at a grid size of 1–2 km to study the convective processes leading to the generation of tropical storms [*Kieu and Zhang*, 2008].

[3] Cloud-resolving and GCM communities have put forth considerable effort over the past decades to examine the model sensitivity to different horizontal grid resolutions. For example, *Petch et al.* [2002] found that finer resolution represents better small-scale "turbulence" to more reasonably capture the timing of initiation and subsequent evolution of both shallow and deep convection. *Bélair and Mailhot* [2001] showed that an explicit condensation scheme with a grid size of 2 km produces more realistically the rainfall and

mesoscale structures of a squall line as compared to lower-resolution runs with parameterized convective schemes. In particular, *Mass et al.* [2002] pointed out that, although real-time NWP models do not show overall superior performance of higher grid resolutions due to the sparseness of station observations, increasing grid resolutions does improve the realism of the structures and evolution of some weather events. In contrast, evaluation of the model sensitivity to horizontal resolution for GCMs is more complicated because of the different characteristics of regional climate. Nevertheless, *Sperber et al.* [1994] and *Jha et al.* [2000] found that higher-resolution GCMs perform better in the simulations of the Indian and East Asian summer monsoon rainfall, and *Senior* [1995] showed that the use of higher resolutions generally produces more favorable changes in climate prediction. Thus, it is generally believed that increasing horizontal resolution with better physics parameterizations will improve the overall performance of numerical models.

[4] It is well known that one of the initial objectives for the development of regional climate models (RCMs) is to make up the coarseness limitation of GCMs through better resolution of local topography and land use. In fact, many studies have demonstrated that RCMs could indeed capture more detailed and reasonable regional climate scenarios than those by GCMs [*Giorgi et al.*, 1994; *Jones et al.*, 1995; *Chen and Fu*, 2000; *Ju and Wang*, 2006; *Gao et al.*, 2008; *Salathé et al.*, 2008]. During the past two decades, many complicated physics processes and aerosol-chemistry modules have been incorporated into RCMs [*Qian and Giorgi*,

[1] LASG, Institute of Atmospheric Physics, Chinese Academy of Sciences, Beijing, China.
[2] Department of Atmospheric and Oceanic Science, University of Maryland, College Park, Maryland, USA.

1999; *Lu et al.*, 2001; *Qian et al.*, 2003; *Wang et al.*, 2003; *Zakey et al.*, 2008] but most of them have kept the horizontal grid sizes around 60 km. In contrast, many NWP models have quickly progressed to grid sizes of 1–5 km during the same time period that have become small enough to resolve the inner-core structures of mesoscale convective systems (MCSs) [e.g., *Done et al.*, 2004; *Kieu and Zhang*, 2008].

[5] Despite weak interest in increasing the grid resolution for most RCMs, some sensitivity tests did indicate that increasing horizontal resolution could improve the simulation results, especially for those heavy rainfall events. For instance, *Xue et al.* [2007] showed that RCMs could produce better the rainfall distribution over North America when the grid size is reduced from 80 to 32 km. *Lee et al.* [2004] found improved heavy rainfall patterns and amounts associated with the June 1998 East Asian flood through the better-simulated downward solar radiation, latent heat flux, and convective rainfall after the grid size was reduced from 60 to 20 km. Similarly, *Im et al.* [2006] obtained better simulations of the present climate over Korea when the RCM grid size was decreased from 60 to 20 km. *Gao et al.* [2006] and *Tang et al.* [2006] found improved rainfall in higher-resolution RCM runs for a 5 year continuous simulation of East Asian rainfall and an extreme rainfall case along the Yangtze River Basin (YRB). However, in all of the aforementioned sensitivity tests, the finest grid size they used was 15 km, i.e., by *Tang et al.* [2006]. To our knowledge, few studies, including both the RCM validation and sensitivity simulations, have used a grid size of less than 10 km to simulate East Asian regional climate, except that of *Liu et al.* [2008]. This is certainly not compatible with the rapid progress in studying MCSs with high-resolution NWP models.

[6] *Liu et al.* [2008] successfully performed a 54 day continuous simulation of the heavy rainfall events over the middle to lower reaches of the YRB (YRB-ML) during the summer of 1998 using the nonhydrostatic version of the Pennsylvania State University-National Center for Atmospheric Research mesoscale model (i.e., MM5) with the finest grid size of 4 km and sophisticated model physics schemes. Results show that the MM5 reproduces reasonably well the daily to submonthly weather and climate characters during the two Meiyu rainy phases (12–30 June and 20–31 July) and the transition period in between (1–19 July). Because of its rainfall severity and sustained period and coverage, several RCM studies have been carried out in an attempt to gain insight into the processes leading to the flooding rainfall production [e.g., *Wang et al.*, 2003; *Lee et al.*, 2004; *Leung et al.*, 2004; *Hsu et al.*, 2004]. However, among the other differences, because of the use of much lower grid resolutions (~60 km) than that used by *Liu et al.* [2008], these RCM simulations contain pronounced errors, and they fail especially to reproduce the observed mesoscale circulations and heavy rainfall during the second Meiyu rainy phase (see *Liu et al.* [2008] for more details).

[7] In view of the growing interest in high-resolution RCMs, the objectives of this study are to (1) evaluate the sensitivity of the RCM-simulated summer 1998 heavy rainfall to horizontal grid resolution in terms of the rainfall intensity and distribution; (2) explore the larger-scale conditions that are favorable for and the physical processes

leading to the generation of excessive rainfall or numerical point storms (NPSs) in lower-resolution simulations; and (3) examine why the summer 1998 heavy rainfall, especially during the second rainy phase, tends to be poorly simulated with lower-resolution RCMs. These objectives are achieved by using the high-resolution simulated summer 1998 heavy rainfall events presented by *Liu et al.* [2008] as the control run.

[8] Section 2 briefly describes the numerical model used for this study and the experimental design. Section 3 presents validation of the control simulation and intercomparisons between the sensitivity simulations with different grid resolutions. Section 4 shows the impact of horizontal resolution on the generation of excessive rainfall events and NPSs during the second Meiyu rainy phase. The effects of NPSs and excessive rainfall on the structures and orientation of the Meiyu front is also discussed. Section 5 discusses why excessive rainfall tends to occur during the second rainy phase and relates the results obtained herein to those shown in the previous case studies. A summary and concluding remarks are given in section 6.

2. Model Description and Experiment Design

[9] In this study, the MM5 is used as an RCM to examine the effects of varying horizontal resolution on the regional climate simulation of the summer 1998 extreme rainfall events along the YRB-ML. The model setups are the same as those by *Liu et al.* [2008], except for the grid size used for the domain covering the major rainfall areas. Three sensitivity tests are conducted with the following resolutions (see Figure 1): (1) 36 km throughout the large domain DO1 (EX_36), (2) adding a nested domain DO2 with the finest grid size of 12 km into DO1 (EX_12), and (3) adding a third nested domain DO3 with the finest grid size of 4 km into DO2 (EX_4). EX_4 is referred to as the control run [see *Liu et al.*, 2008].

[10] The model water cycles used for this study include (1) a simple ice microphysics scheme for grid-scale precipitation with the prognostic equations for cloud water, cloud ice, rain water, and snow [*Zhang*, 1989; *Dudhia*, 1989]; (2) the newest version of the Kain-Fritsch (KF2) convective parameterization scheme (CPS) for subgrid-scale convection including the effects of shallow convection [*Kain*, 2004]; (3) the Eta model's Mellor-Yamada planetary boundary layer (PBL) scheme [*Janjić*, 1994]; (4) a long- and short-wave radiation scheme which interacts with the atmosphere, cloud, and land surface [*Dudhia*, 1989]; and (5) the land surface model of the National Centers for Environmental Prediction (NCEP)-Oregon State University-Air Force-Hydrologic Research Lab [*Chen and Dudhia*, 2001a, 2001b]. All the nested domains are two-way interactive with the same physics schemes (see *Zhang et al.* [1986] for a detailed description of the nesting procedures).

[11] Note that a CPS was also used by *Zhang et al.* [2003] in their finest-grid 5 km RCM study. In our view, a CPS is still needed for RCMs with 3–5 km horizontal resolutions, because they could not resolve even the largest supercell storms of about 6–10 km, especially the associated intense updrafts at the scales of 1–2 km. We conducted the same run as EX_4, but without a CPS for a short period of integration, and found the development of NPSs similar to those
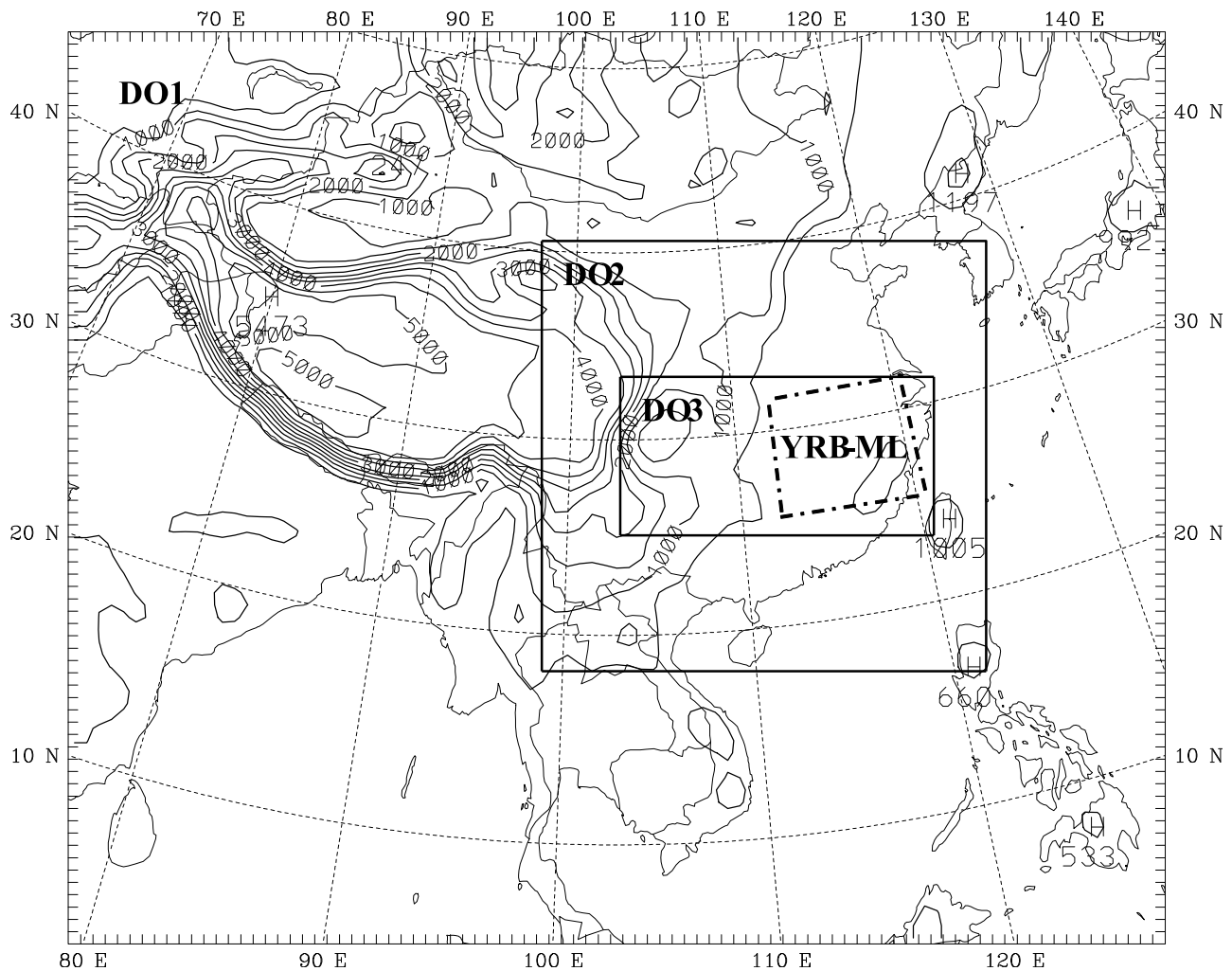
Figure 1. Model domains of three sensitivity simulations (and the model topography at intervals of 500 m): only one domain for EX_36 (DO1), two nested domains for EX_12 (DO1 and DO2), and triply nested domains for EX_4 (DO1, DO2 and DO3). The interior box (dot-dashed) denotes the YRB-ML region (i.e., 26–32°N, 113–121°E).

discussed by *Zhang et al.* [1988], *Molinari and Dudek* [1992], and *Zhang et al.* [1994]. This finding implies that upward motion developed on the 4×4 km^2 grid box still could not remove potential instability fast enough to prevent the development of a conditional instability of the second kind.

[12] The model initial conditions and outermost lateral boundary conditions for all three sensitivity tests are specified from the NCEP/Department of Energy 6 hourly, 2.5° resolution Reanalysis-2 (R-2) data [*Kanamitsu et al.*, 2002]. To provide an appropriate large-scale forcing, we adopt a buffer zone of about 1000 km (30 grid intervals) at the outermost lateral boundaries, following *Wang et al.* [2000, 2003] and *Leung et al.* [2004]. The initial soil variables are from the European Centre for Medium-Range Weather Forecasts 40 year reanalysis (ERA-40), which are nudged toward the observed screen-level temperature and humidity [*Kållberg et al.*, 2004]. Although it is desirable to use an atmosphere-ocean coupled RCM to simulate the sea surface temperature (SST) field, it is obtained herein by linearly interpolating in both time and space the Reynolds weekly SST at 1° resolution [*Reynolds and Smith*, 1994]. The model

is initiated at 0000 UTC 8 June 1998 and then continuously integrated to 1800 UTC 31 July 1998. The first 4 day integrations are treated as the model spinup, so they are not used for the model analysis. During the 54 day simulation period, the lateral boundary conditions and SST are updated every 6 h. There are 34 σ levels in the vertical and the model top is set at 50 hPa (see *Liu et al.* [2008] for more details).

3. Results

[13] Because of the two-way interaction of the nested domains, the model results from finer meshes of each simulation do not differ significantly from those in coarser meshes over their overlapped regions. Thus, all the sensitivity simulations that follow are compared to the control run over the same subdomain of DO1, and any difference between them can be attributed to the effects of using different resolutions. Moreover, more attention is paid to rainfall distribution and intensity along the YRB-ML and low-level regional circulations because of little differences
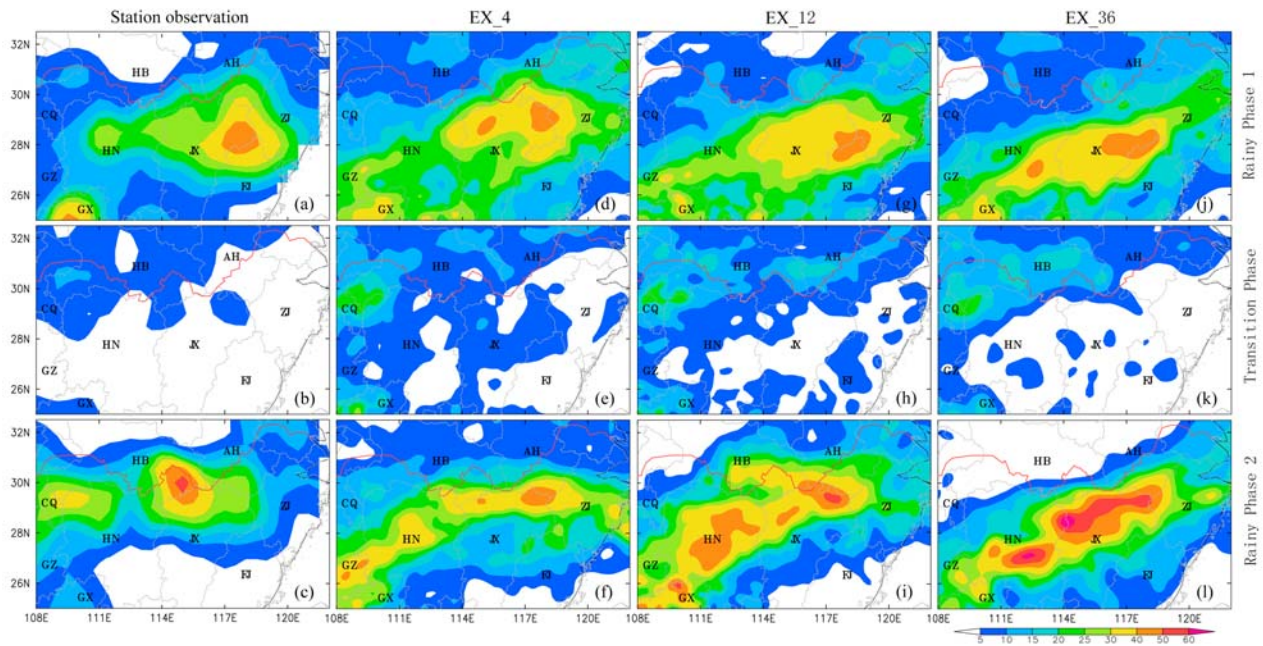
Figure 2. Horizontal distribution of the averaged daily rainfall rates (mm d^{-1}) from (a–c) the station observations, (d–f) EX_4, (g–i) EX_12, and (j–l) EX_36 over a subdomain of DO1 for the periods 12–30 June (rainy phase 1), 1–19 July (transition phase), and 20–31 July (rainy phase 2) 1998. Provincial boundaries (light shaded lines) and Yangtze River (red line) are shown. Provinces are denoted as follows: GZ, Guizhou; HB, Hubei; CQ, Chongqing; AH, Anhui; FJ, Fujian; ZJ, Zhejiang; HN, Hunan; JX, Jiangxi; GX, Guangxi.

in the simulations of large-scale circulations among all the runs (not shown).

3.1. Rainfall

[14] Figure 2 compares the total rainfall from the two sensitivity simulations to the control-simulated run during the two Meiyu rainy phases and the transition period in between; the observed rainfall is also included to facilitate the comparisons. It is evident that all the simulations show similar rainfall patterns, including a major rainbelt over the YRB-ML, its northwestward advancement, and a southward retreat to the YRB region during the first rainy phase, the transition, and the second rainy phase, respectively. These results are expected because the general distribution of the Meiyu frontal rainfall is more or less controlled by the large-scale circulations that are similar among all the simulations.

[15] However, there are obvious differences in rainfall intensity and the location of rainfall centers, especially during the second rainy phase (cf. Figures 2f, 2i, and 2l). Specifically, EX_4 reproduces reasonably well the rainfall centers near the borders of Zhejiang (ZJ), Fujian (FJ), and Jiangxi (JX) provinces and over the north-central JX and the northern Guangxi (GX) provinces during the first rainy phase (cf. Figures 2d and 2a). The near meridionally distributed rainfall tail from GX to Hunan (HN) provinces is also reasonably simulated, though with notable rainfall underprediction over northern HN. Although both EX_12 and EX_36 better reproduce the rainfall center near the ZJ-FJ-JX borders, the simulated major rainfall belts are shifted more southward, especially for the southwest portions (cf. Figures 2g, 2j, and 2a). During the transition phase, all the

three simulations produce similarly light rainfall, except that the intensity increases by 5 to 10 mm d^{-1} along the YRB-ML as the grid size increases (cf. Figures 2e, 2h, and 2k).

[16] Although all the simulations failed to mimic the heavy rainfall over the middle portion of the YRB during the second Meiyu rainy phase, EX_4 could still reproduce reasonably well an east-west-oriented rainbelt along the YRB-ML even 54 days into the integration. By comparison, the east-west-oriented rainbelt gradually becomes northeast-southwest oriented in EX_12 to EX_36 (cf. Figures 2c, 2f, 2i, and 2l). Of interest is that the total rainfall amounts along the rainbelt are much larger than those in EX_4; they are more than 50% at some rainfall centers. For instance, the heavy rainfall in northern JX and southern HN in EX_36 is 10–20 mm d^{-1} larger than that in EX_4 and EX_12. The increased total (or excessive) rainfall, as the grid resolution is reduced, is often unexpected, which reveals some potential problems with the model physics parameterizations (as explored in section 4). In addition, the observed heavy rainfall center near the borders of Chongqing (CQ), Guizhou (GZ), and HN provinces is displaced more to the southeast from EX_4 to EX_12 and EX_36. In general, the three simulations plus our experimental simulations (not shown) reveal that the simulated rainbelts occurring during the 1998 Meiyu season tend to be shifted southward and their intensities increase as the grid resolution decreases. As shown in section 4, this phenomenon is mainly caused by the subgrid and grid-scale interactions of cloud and precipitation processes leading to the development of excessive rainfall or NPSs.
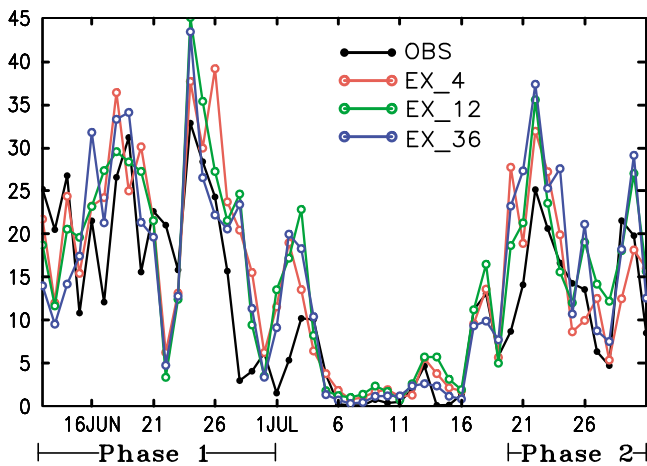
Figure 3. Time series of the daily rainfall rates (mm d^{-1}) averaged over the YRB-ML region from the station observations (black), EX_4 (red), EX_12 (green), and EX_36 (blue) during the period 12 June to 31 July 1998.

[17] Figure 3 compares the time series of the simulated daily rainfall rates over the YRB-ML region with the three different grid resolutions. In general, all the simulations capture well the major rainfall events. Again, EX_12 and EX_36 produce large positive rainfall biases during the second Meiyu rainy phase (e.g., on 22, 26, and 30 July), which is consistent with the data shown in Figure 2. On average, EX_4, EX_12, and EX_36 exhibit a positive biases of 2.9, 4.9, and 6.2 mm d^{-1} during this rainy phase, respectively.

[18] To further explore the influence of horizontal grid resolution on regional climate, Figure 4 compares the parameterized and grid-scale rainfall during the two Meiyu rainy phases from the three simulations. Of significance is that the grid-scale precipitation accounts for a large portion of the total rainfall in all the runs because of the continuous mesoscale ascent of moist monsoonal flows over the Meiyu front. It is well known that, as the grid size increases, the grid-scale precipitation should decrease because some of the associated physics processes (e.g., updrafts and downdrafts) become subgrid-scale phenomena and are treated implicitly by CPSs [Zhang et al., 1988, 1994; Bélair and Mailhot, 2001]. Indeed, Figures 4a, 4e, 4i, 4b, 4f, and 4j indicate that the parameterized (grid-scale) rainfall does increase (decrease) during the first rainy phase as the horizontal resolution decreases from EX_4 to EX_12 and EX_36. Similarly, the grid-scale rainfall decreases in percentage from more than 90% in EX_4 to about 60% in EX_12 and EX_36.

[19] The grid-scale rainfall during the second rainy phase still accounts for a sizable portion (60–70%) of the total
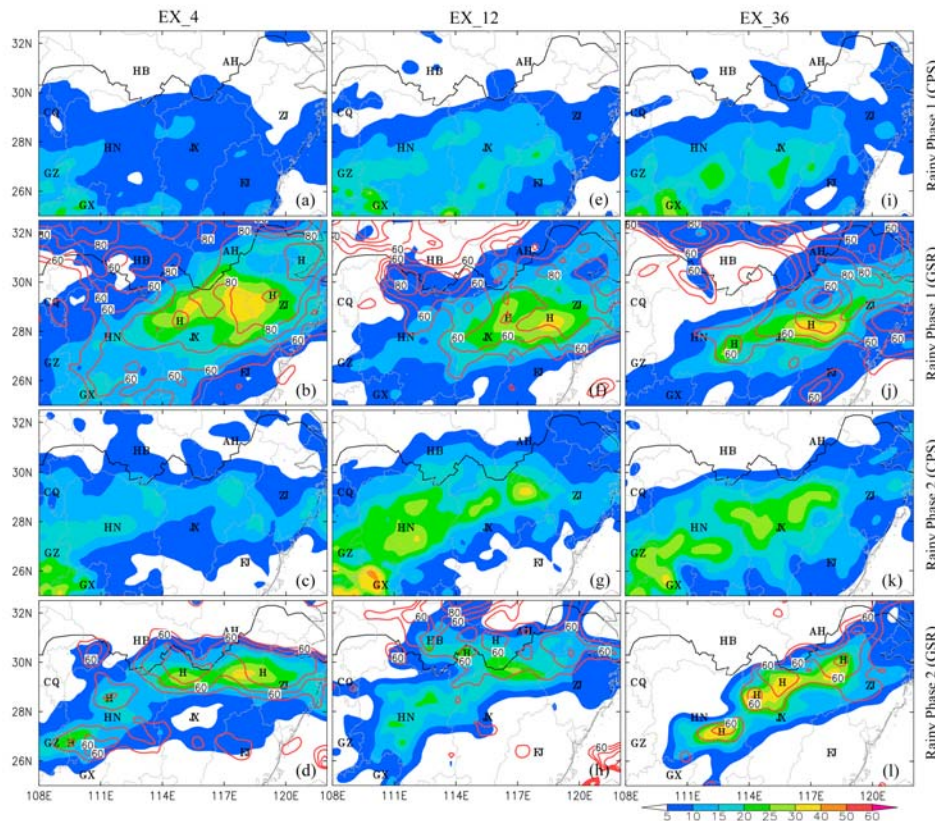

Figure 4. Horizontal distribution of (a, c, e, g, i, k) the averaged daily subgrid-scale rainfall rates (CPS, mm d^{-1}) and (b, d, f, h, j, l) the averaged daily grid-scale rainfall rates (GSR, mm d^{-1}) and the percentage of GSR (red, at intervals of 10%) from EX_4, EX_12, and EX_36 for the periods 12–30 June 1998 (Figures 4a, 4b, 4e, 4f, 4i, and 4j) and 20–31 July 1998 (Figures 4c, 4d, 4g, 4h, 4k, and 4l).

rainfall (cf. Figures 4c, 4g, 4k, 4d, 4h, and 4l), but it is significantly less than that during the first rainy phase. This result is consistent with the rainfall analysis of *Liu et al.* [2008], who showed that the second rainy phase was more convectively dominated with the propagation of several MCSs along the YRB-ML region. Of relevance to this study is that despite the use of different grid resolutions both the parameterized and the grid-scale rainfall amounts are greater in lower-resolution runs than those in higher-resolution runs, and the grid-scale rainfall in all the simulations accounts for a similar percentage of the total rainfall, only slightly more in EX_4. Moreover, more localized rainfall occurs in lower-resolution runs (e.g., Figures 4g, 4k, and 4l). These results imply further the importance of the interaction of parameterized and grid-scale convective processes in treating convectively unstable columns and in reproducing the observed heavy rainfall [see *Zhang et al.*, 1994; *Bélair and Mailhot*, 2001].

[20] On the basis of the aforementioned results, we may state that in the present case the RCM tends to improve the regional climate simulations of heavy rainfall events in both the distribution and the amounts as the horizontal grid resolution increases. In addition, the parameterized and grid-scale rainfall could be better treated in higher-resolution models, and similarly for the other regional climate features: surface temperature, horizontal winds, and cloud amount (not shown).

3.2. Low-Level Circulations

[21] Before addressing the different roles of parameterized and grid-scale physical processes in generating the heavy rainfall events, it is necessary to examine how the overpredicted rainfall in the lower-resolution simulations would result in the low-level circulations as compared to the observed values. Because of the larger rainfall differences among the three resolution simulations, we next focus on the second Meiyu rainy phase.

[22] Figure 5 compares the distribution and magnitudes of (12 day averaged) horizontal winds and equivalent potential temperature (θ_e) at 850 hPa from the three simulations to the R-2 reanalysis; the latter is treated here as the best estimate of the "atmospheric true state." One can see several common features from Figure 5: (1) a meso-α-scale cyclonic circulation over the Yellow Sea, denoted by L, (2) a strong southwesterly monsoonal flow over south China that converges with a northeasterly flow along the YRB, and (3) a high-θ_e tongue extending from southwest China to the YRB-ML with large north-south gradients corresponding to the distribution of the Meiyu front. However, there are some obvious differences among these features. First, the Yellow Sea cyclone appears to be stronger than the observed values in all the simulations, and its intensity and area coverage become greater in lower-resolution simulations. Second, the area coverage of the southwesterly flow larger than 12 m s^{-1} is larger in lower-resolution simulations, with its core region shifting toward China's southeastern coast; that is, EX_12 produces the strongest southwesterly wind of 16 m s^{-1}, compared to 12 m s^{-1} in both the EX_4 simulation and the R-2 analysis (cf. Figures 5a–5c). Third, as a result of the simulated stronger cyclones over the Yellow Sea, lowerresolution results show stronger northeasterly flows. For instance, both the R-2 analysis and the EX_4 simulation

exhibit northeasterly to easterly flows to the north of the YRB-ML that converge slightly with the southwesterly monsoonal flow (Figures 5a and 5b), whereas both EX_12 and EX_36 produce a significant convergence zone between the two airstreams along the Meiyu front (Figures 5c and 5d); the northeasterly flows in both cases are even displaced to the south of the YRB. Clearly, the stronger the northeasterly and southwesterly flows, the more water vapor over the ocean surface of the Yellow Sea and the South China Sea can be transported into the Meiyu frontal region in lower-resolution runs, especially EX_36.

[23] Figure 6 compares the 12 day averaged sea-level pressure field from the three simulations to the R-2 analysis. In general, the larger-scale pressure patterns are all similar during the second rainy phase, especially the southwestnortheast-oriented low-pressure zones. The lower pressure zone in EX_4, extending from the Yellow Sea to the YRB-ML and Guizhou Province, compares favorably to the R-2 analysis in terms of both the minimum pressure and the mean pressure gradients (cf. Figures 6a and 6b). However, its intensity from both EX_12 and EX_36 appears 1–2 hPa stronger than the observed, similar to that for the pressure gradients (cf. Figures 6c, 6d, and 6a). The lower-pressure coverage is also greater than that in EX_4 and the R-2 analysis.

[24] The preceding results are all consistent with the development of stronger low-level southwesterly and northeasterly flows (Figure 5) and excessive rainfall (Figure 2) in south China, as the model grid resolution decreases from 4 km to 12 and 36 km. Clearly, it is the positive feedback between latent heat release, low-level moisture convergence, and surface pressure decrease that are responsible for the development of excessive rainfall in lower-resolution simulations. Two natural questions one may ask are: Why is such a positive feedback more pronounced in lowerresolution simulations? How does the Meiyu front or the broad pressure trough system tend to be southwest-northeastoriented as the grid resolution decreases? These are the subjects of our study in section 4.

4. Development of Excessive Rainfall

[25] The preceding questions can be addressed by examining the mechanisms by which excessive rainfall occurs in lower-resolution simulations. For this purpose, we traced each major rainfall event at higher temporal resolutions from the three simulations and found that more strong, longlasting MCSs with excessive rainfall tend to appear in lower-resolution simulations, especially in EX_36; some of them are essentially originated from NPSs [*Zhang et al.*, 1988, 1994; *Giorgi*, 1991].

[26] Figure 7 shows three representative events of excessive rainfall simulated from EX_36 that occur during the following three 15 h periods of the second rainy phase: 1200 UTC 21 July to 0300 UTC 22 July, 0900 UTC 23 July to 0000 UTC 24 July, and 2100 UTC 25 July to 1200 UTC 26 July 1998; they are also compared to the MCSs simulated in EX_4 and the station observations. We can see that EX_4 reproduces reasonably well the flow patterns and intensities at 850 hPa, including an MCS (denoted as A) with a closed meso-α-scale cyclone (or mesolow) later over the Yellow Sea (cf. Figures 7 and 5), a mesolow (denoted as D) to the
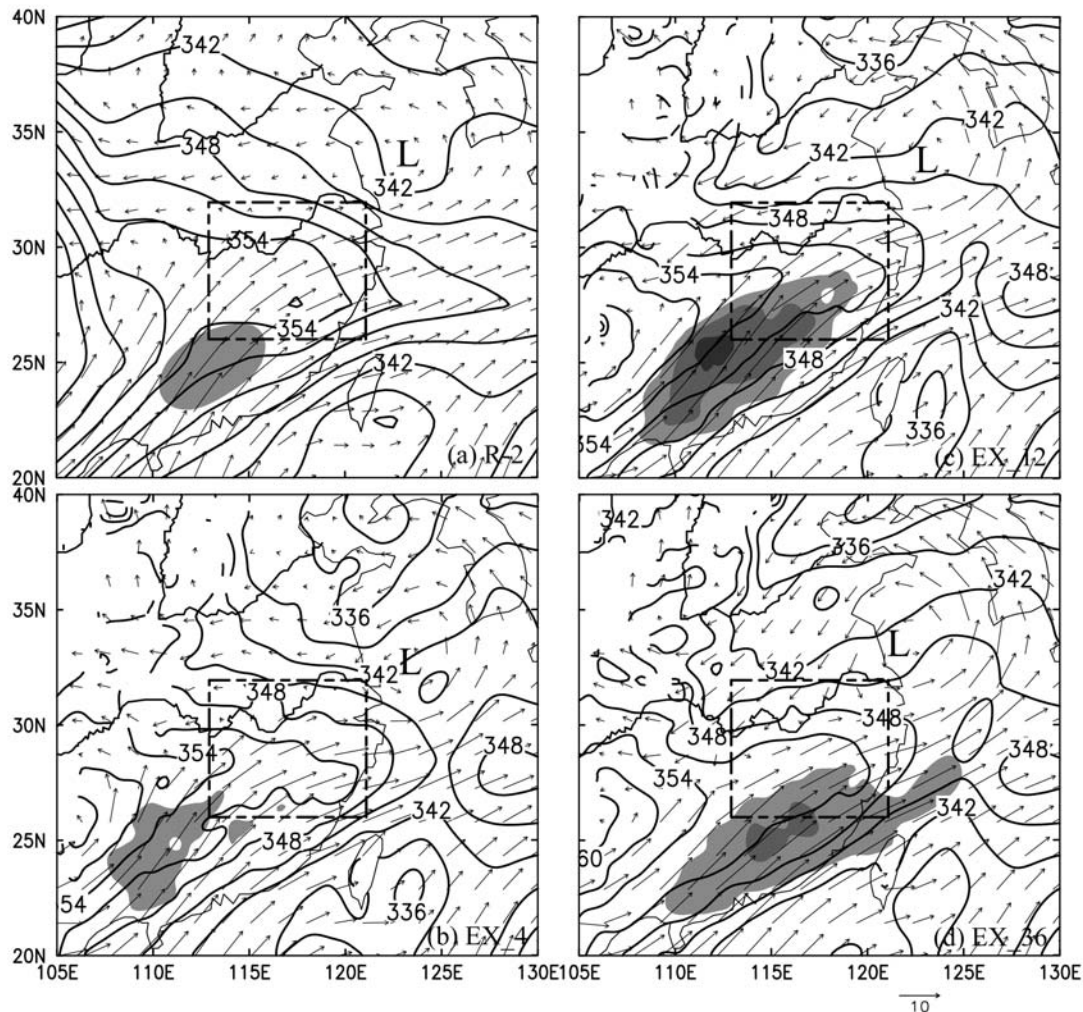
Figure 5. Horizontal distributions of 850 hPa wind vectors (m s^{-1}) and equivalent potential temperature (θ_e, solid lines at intervals of 3 K) from (a) the R-2 reanalysis, (b) EX_4, (c) EX_12, and (d) EX_36 that are averaged during the second rainy phase (20–31 July). Shadings, at intervals of 2 m s^{-1}, denote wind speeds greater than 12 m s^{-1}. The interior box denotes the YRB-ML region.

southwest, a weak deformation zone between A and D, and a higher-pressure zone (denoted as H) to the north, compared to the R-2 analysis (cf. Figures 7a–7c and 7d–7f). The associated precipitation during the three time periods is also reasonably simulated, especially considering that the results are from the model simulations beyond 40 days. Although EX_4 appears to "overpredict" a couple of small mesolows offshore (see Figures 7d and 7e), they could not be verified because of the lack of high-resolution observations in the R-2 analysis.

[27] In contrast, EX_36 overpredicts the MCS A starting from its early stage (cf. Figure 7g and Figures 7a and 7d) and produces one "fictitious" intense mesolow B that does not resemble any system in EX_4 or R-2 (cf. Figure 7h and Figures 7b and 7e), and one unrealistic mesolow C (cf. Figure 7i and Figures 7c and 7f). Their associated excessive rainfall amounts are also evident, with the 15 h accumulated amount reaching 310 mm for A and 170 mm for B and C, and they account for the excessive rainfall amounts during the corresponding periods shown in Figures 2–4. Mesolow

C is considered unrealistic because its origin is similar to mesolow D in EX_4 and the R-2 analysis, just at slightly different locations, but its subsequent evolution appears to be erroneous (see Figures 8 and 10). Specifically, mesolow C begins to move northeastward along the Meiyu front after forming a closed circulation, and it is eventually absorbed by system A after moving offshore; the behavior of the fictitious system B is similar (not shown). However, mesolow D in EX_4 remains quasi-stationary, nearly like the observed one, for another 2–3 days. Clearly, these different scenarios among B, C, and D have been "smoothed out" or obscured after temporal averages of just a couple days in regional climate studies [e.g., *Liu et al.*, 2008]. The northeastward displacement of mesolow B may be attributed to the attraction of the intense mesolow A, and later C attracted by B, through mass convergence in the PBL and the presence of stronger southwesterly flows in the southwest-northeast-oriented broader trough in EX_36. It is our belief that most of the differences between EX_4 and EX_36 result from the
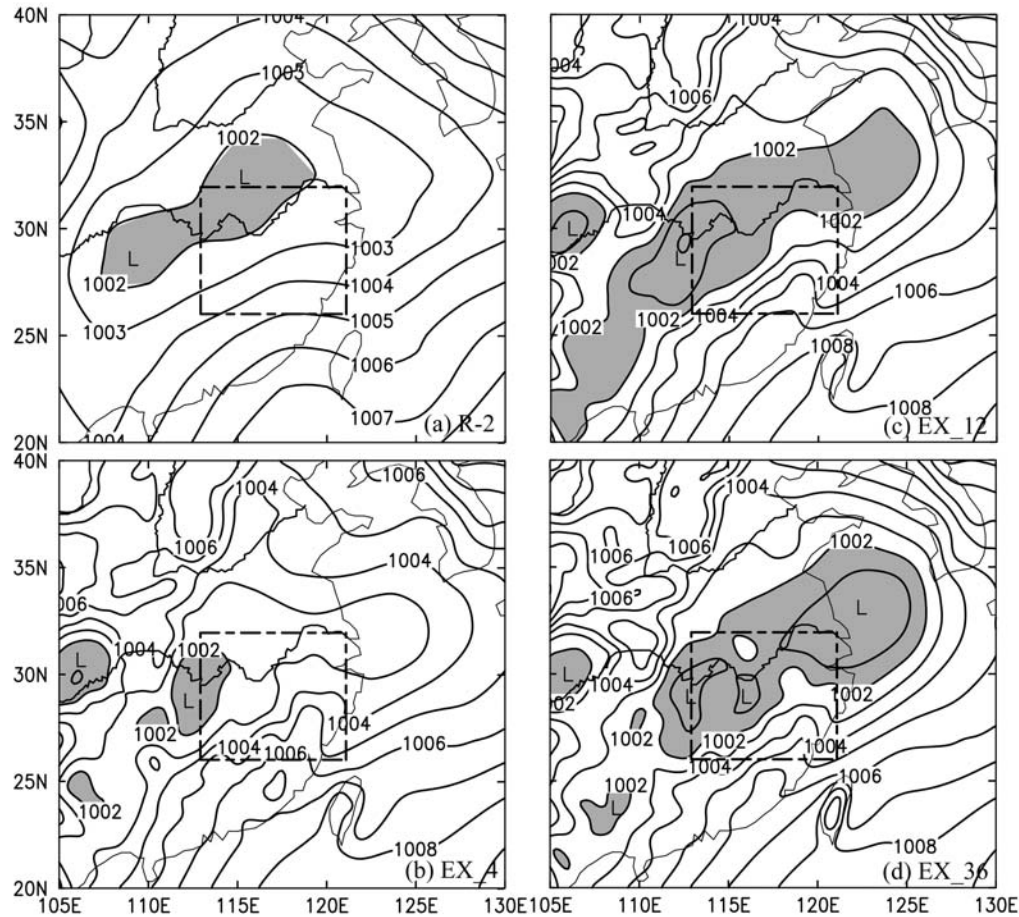
Figure 6. As in Figure 5 but for the sea-level pressure field at intervals of 1 hPa. Pressure values lower than 1002 hPa are shaded.

generation of the too-intense MCS A and of the fictitious storm B.

[28] Moreover, because of the excessive amount of latent heat release, the strong mesolow A in EX_36 becomes longer lived after moving offshore; it lasts for 3–4 days (e.g., from 0000 UTC 21 July to 0000 UTC 25 July) with the minimum pressure deficit of about 6–8 hPa deeper than that in EX_4 (Figure 8). As a result, more cold and dry air masses are transported southward by the intense cyclonic flows such that the western portion of the Meiyu front is pushed south- to southwestward, unlike the nearly east-west-oriented frontal system as in EX_4 (cf. Figures 7h, 7i and Figures 7e, 7f). Thus, we may state that the development of the too-strong mesolow A (and too-excessive rainfall associated with systems B and C) most likely accounts for the southwestward displacement of the Meiyu front during the second rainy phase as shown in Figures 5 and 6. Obviously, such excessive developments must be minimized to obtain more realistic analyses of regional climate and weather conditions.

[29] To help understand why the excessive rainfall develops in the aforementioned mesolows, Figure 9 shows the temporally averaged θ_e and flow vectors at 850 hPa, superimposed with the accumulated rainfall during the three different periods. One can see that a high-θ_e tongue, asso-

ciated with the warm and moist southwesterly flows, is located to the south of the Meiyu front, and excessive rainfall events tend to be initiated locally in higher-θ_e (355–360 K at 850 hPa) regions. Of interest is that, after the formation of a mesolow as a result of rapid latent heat release, the energy supply to the MCSs located downstream are blocked. For example, mesolow B (and C) consumes most of the high-θ_e air in the southwesterly flows, so only a small amount of latent energy can be transported to the systems to the northeast (cf. Figures 7h, 7i and Figures 9b, 9c); the southwesterly energy supply to system A is even cut off because of its cyclonic advection of the lower-θ_e air from the northeast (Figure 9c). As a result, the upstream systems are amplified, with the tremendous grid-scale condensation occurring near the low-pressure centers, whereas the downstream systems may maintain their intensity or slowly decay with the much less grid-scale latent heat that is released in the southwesterly flow. It is evident from Figures 7 and 9 that the grid-scale rainfall accounts for more than 80% of the total accumulated rainfall at all the rainfall centers in EX_36. On the basis of the previous studies [e.g., *Zhang et al.*, 1988, 1994], such a large percentage of grid-scale rainfall implies that the CPS used is inefficient to remove the potential instability generated by a larger-scale energy supply. Thus, more attention must be paid to the impact of
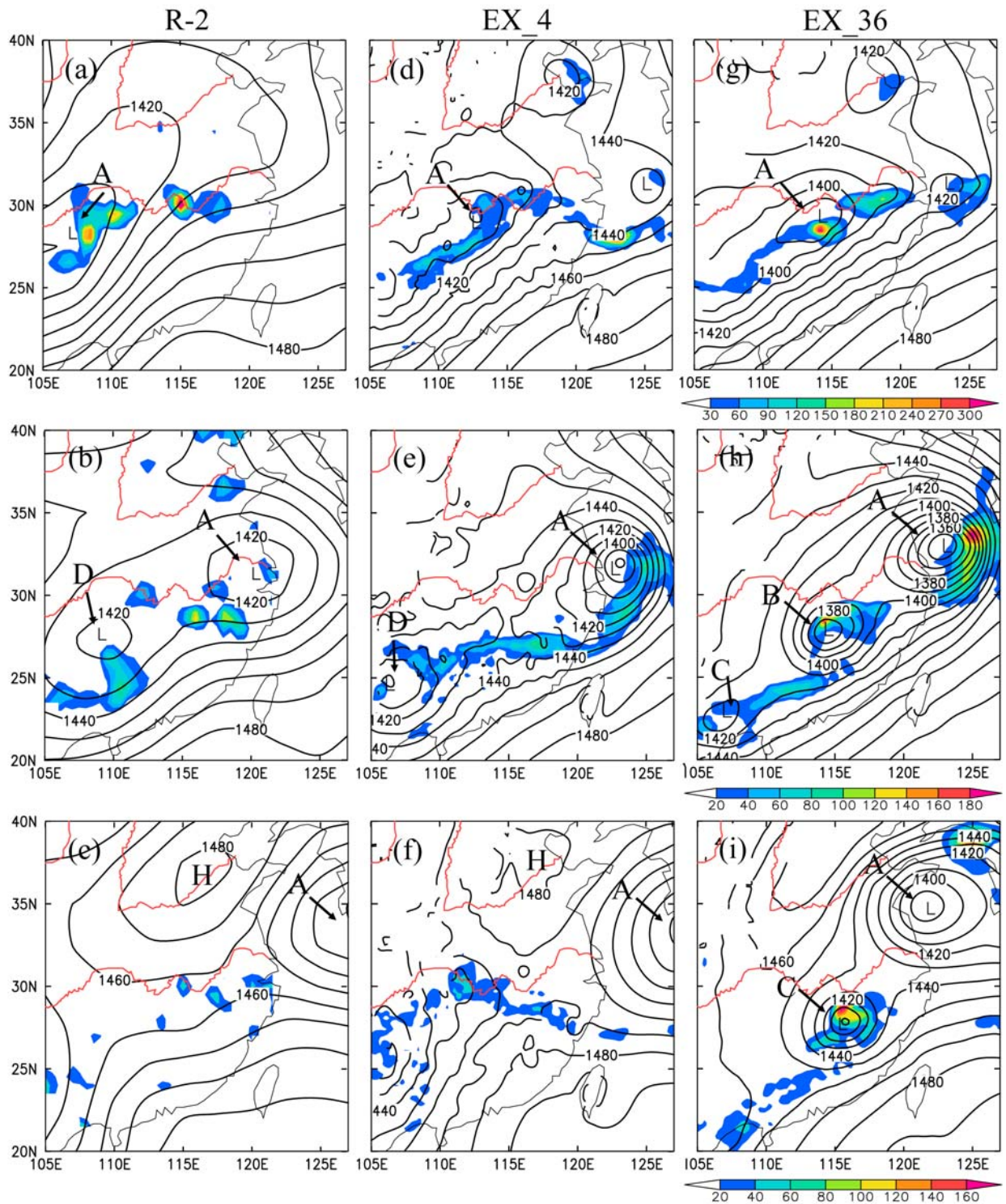
Figure 7. The 850 hPa averaged geopotential height (solid lines at intervals of 10 m) and the accumulated total rainfall (shaded, mm) from (a–c) the station observations (for rainfall) and the R-2 analysis (for geopotential height), (d–f) EX_4, and (g–i) EX_36 during the periods of 1200 UTC 21 July to 0300 UTC 22 July (top row), 0900 UTC 23 July to 0000 UTC 24 July (middle row), and 2100 UTC 25 July to 1200 UTC 26 July (bottom row) 1998. The letters A–D represent different mesolow pressure systems.
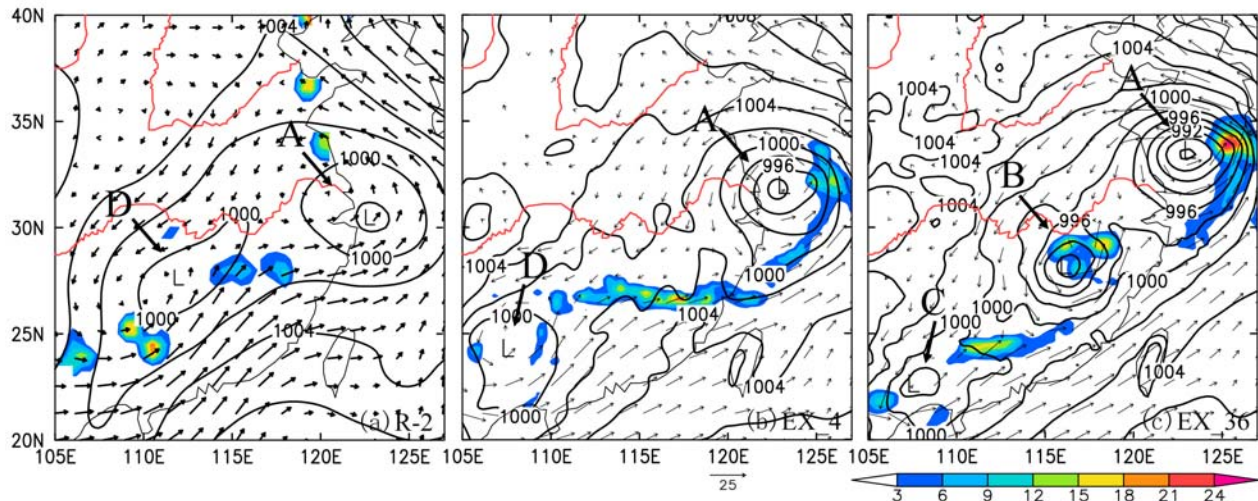
Figure 8. As in Figure 7 but for the sea-level pressure (solid lines at intervals of 2 hPa), 850 hPa wind vectors (m s^{-1}), and the hourly rainfall rates (shaded, mm h^{-1}) at 0000 UTC 24 July 1998 from (a) the R-2 and station observations, (b) EX_4, and (c) EX_36.

CPSs in higher-θ_e regions upstream in the southwesterly monsoonal flows to minimize the generation of too-excessive rainfall or NPSs associated with the Meiyu front.

[30] Figure 10 shows an example of the larger-scale environment in which the excessive rainfall associated with the fictitious storm B is generated compared to the conditions appeared in EX_4. It is evident that the aforementioned mesolows are associated with closed cyclonic circulations with locally stronger southwesterly winds on the southern side of the Meiyu front. This is particularly true for the mesolows and deeper Meiyu-frontal trough in EX_36 caused by the presence of stronger pressure gradients. This implies that more high-θ_e air tends to be transported into the frontal region for convective develop-ments, providing the necessary energy source for the intensification of the mesolows and frontal trough. Their intensifications involve positive feedback between diabatic heating, surface pressure falls, lower-level transport and convergence of high-θ_e air, and excessive rainfall, which is more pronounced in EX_36 than in EX_4. Figure 10 also shows clearly the southward intrusion of cold and dry (or lower-θ_e) air from the northeast as a result of the more intense frontal trough and mesolow A in EX_36. However, there is little evidence of the northeasterly flows reaching the latitude of 25°N in EX_4 (cf. Figures 10d and 10h).

[31] Despite the different circulation patterns, both EX_36 and EX_4 show that the southwesterly flows are stronger during the evening hours and have the highest intensity near
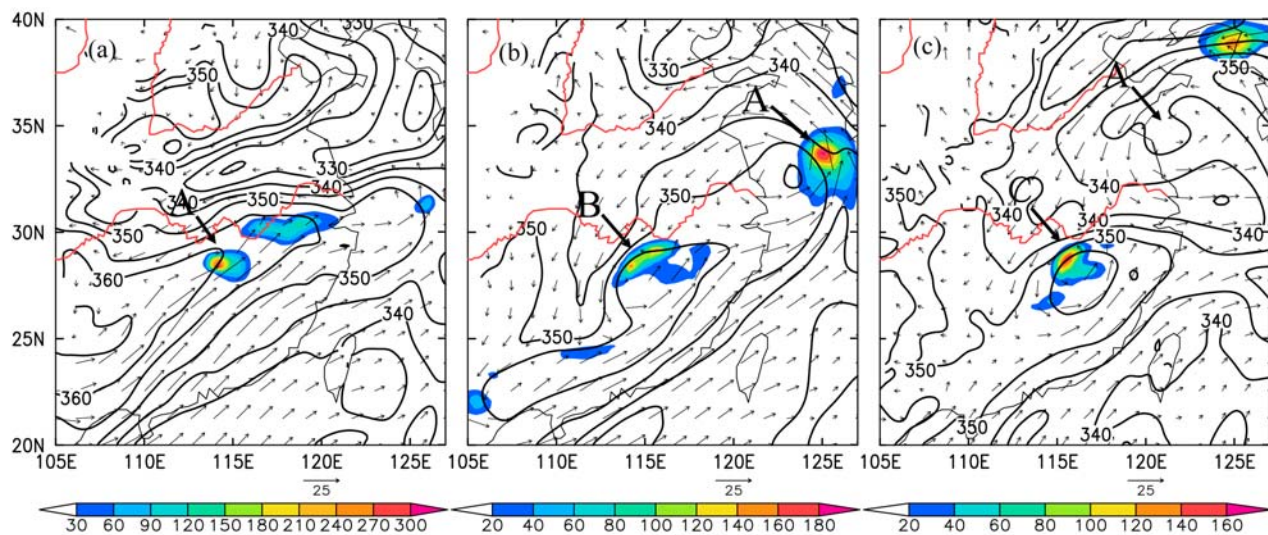

Figure 9. As in Figures 7g, 7h, and 7i but for the 850 hPa equivalent potential temperature (θ_e, solid lines at intervals of 5 K), horizontal wind vectors (m s^{-1}), and the accumulated grid-scale rainfall (shaded, mm) from EX_36.
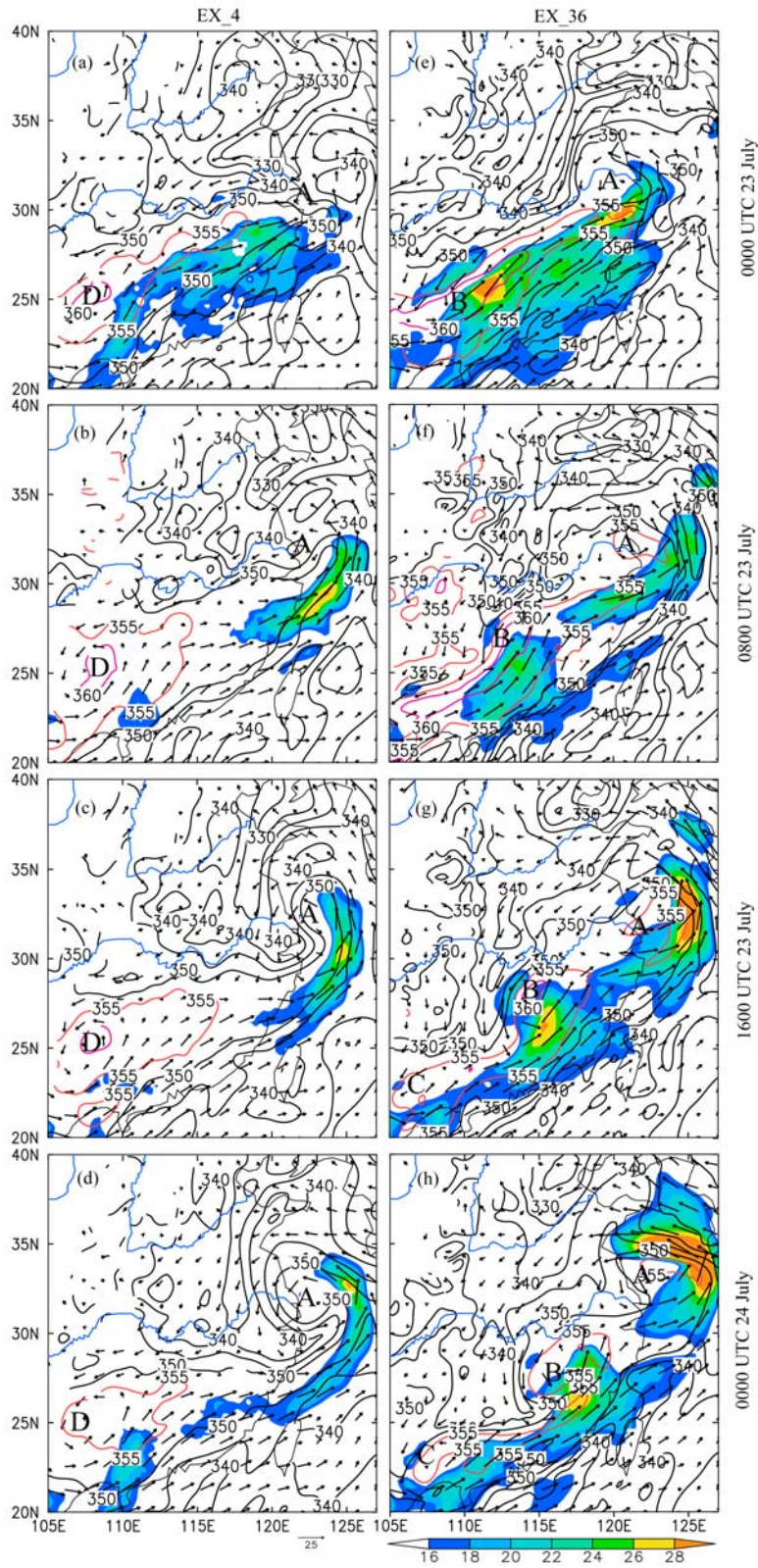
Figure 10. The 850 hPa equivalent potential temperature (θ_e, solid lines at intervals of 5 K) and horizontal wind vectors (m s^{-1}) at 8 h intervals from (a–d) EX_4 and (e–h) EX_36 during the period 0000 UTC 23 July to 0000 UTC 24 July 1998. Wind speeds greater than 16 m s^{-1} are shaded at intervals of 2 m s^{-1}; θ_e values larger than 355 K are shown in red.

0000 UTC (e.g., see Figures 10a, 10d, 10e, and 10h). This coincides with the development of more nocturnal rainfall during the rainy phase [see also *Liu et al.*, 2008, Figures 11 and 12]. Moreover, excessive rainfall associated with the mesolows also exhibits some diurnal variations because of the greater energy supply from the southwesterly flows.

5. Discussions

[32] The generation of excessive rainfall or NPSs in NWP models is well known [e.g., *Zhang et al.*, 1988, 1994; *Giorgi*, 1991; *Molinari and Dudek*, 1991], and it has plagued many NWP modelers for several decades. This problem was early recognized as gravitational instability that is closely related to the (simple) grid-scale latent heat release [*Kasahara*, 1961]. Later, *Zhang et al.* [1988] proposed the use of a full physics (or hybrid) approach, in which both explicit and implicit convective schemes are simultaneously incorporated, to minimize the development of such physical instability for mesoscale NWP models. As discussed by *Zhang et al.* [1994], excessive rainfall or NPSs tend to develop when a CPS is unable to effectively remove the large amount of potential instability in a column and the remaining portion is removed by the grid-scale processes. Because the latter occurs on a time scale much longer than that associated with the CPS, absolute instability may develop in that column in the presence of grid-box saturation, leading to the generation of excessive rainfall and sometimes fictitious intense "cyclonic circulations" (or NPSs). Owing to the development of weaker grid-scale vertical circulations, the lower the horizontal resolution, the higher the probability is for the development of NPSs.

[33] As discussed by *Zhang et al.* [1988], excessive rainfall or NPSs tend to develop in weak-gradient environments. In the present case, these features are not evident during the first rainy phase even in the lower-resolution simulations. On the basis of the results of *Liu et al.* [2008], we may attribute this different rainfall feature to different larger-scale environments and Meiyu frontal circulations during the two rainy phases; that is, more significant baroclinic forcing occurs across the Meiyu front with relatively lower-θ_e air in the southwesterly flows during the first rainy phase than that during the second rainy phase [see *Liu et al.*, 2008, Figure 8]. The associated stronger vertical shear tends to deform the vertical columns of mesolows such that excessive rainfall can be suppressed. Although the grid-scale rainfall accounts for a greater portion of the total rainfall (see Figure 4), it is mostly from stratiform clouds occurring under convectively neutral or stable conditions as the monsoonal flows overrun the Meiyu frontal zone [see *Liu et al.*, 2008, Figures 8a and 8d].

[34] In contrast, most rainfall events during the second phase are thermodynamically driven with much weaker vertical shear but higher potential instability over the YRB-ML region [see *Liu et al.*, 2008, Figures 8c and 8f]. In addition, the Meiyu front during the second phase exhibits stronger horizontal shears in the lower troposphere than that during the first phase [see *Liu et al.*, 2008, Figure 2], so the transformation of the associated shear vorticity to curvature vorticity facilitates the generation of mesovortices (or mesolows). Although the second phase produces a smaller percentage of the grid-scale rainfall than that during the first

phase, it occurs mostly in convectively unstable conditions. It is evident from the discussions in the preceding paragraph that the excessive rainfall or NPSs shown in section 4 can be attributed to the CPS used in EX_36 that fails to remove the buildup of potential instability by the southwesterly flows. On the other hand, the excessive rainfall is much less serious in higher-resolution simulations (e.g., in EX_4) because the simulated relatively stronger grid-scale vertical motion, including the generation of moist downdrafts, could remove convective instability more efficiently than that in lower-resolution simulations. It follows that the development of excessive rainfall or NPSs during the second rainy phase in EX_36 is not caused by the long period of model integration but by the inability of the CPS to remove convectively unstable conditions. This result suggests that different combinations of grid-scale and parameterized convective schemes may be used for different resolutions of RCMs. We may speculate that an RCM with the finest grid size of 4 km but without the KF2 scheme would produce more rainfall than that in EX_4 in the present case.

[35] After obtaining the preceding findings, it would be of interest to examine if similar excessive rainfall and frontal features would appear in the other lower-resolution regional climate simulations of the same case (i.e., the June–July 1998 heavy rainfall events along the YRB-ML), despite the use of different physics schemes therein. We note that, compared to the observed east-west orientation, *Wang et al.* [2003] and *Leung et al.* [2004] also showed the northeast-southwest-oriented Meiyu front in their June 1998 simulations, corresponding to the more simulated rainfall than that observed. Similar results also appear in the simulations of *Lee et al.* [2004] and *Hsu et al.* [2004] during the months of June and July 1998. Note that *Leung et al.* [2004] and *Lee et al.* [2004] used the Grell (1993) CPS, whereas *Hsu et al.* [2004] and *Wang et al.* [2003] used the Kuo type and Tiedtke's CPS, respectively. Hence, the generation of excessive rainfall appears to be a common problem for most CPSs. In addition, *Lee et al.* [2004] and *Hsu et al.* [2004] produced many localized rainfall centers with stronger southwesterly flows during the second rainy phase, similar, to a certain extent, to our EX_36 simulation. Apparently, we may attribute the failure of the previous RCMs in simulating the (first- and) second-phase rainfall to the generation of too-excessive rainfall, likely more NPSs, and too-strong mesolows along or to the northeast of the Meiyu front. We may speculate significant improvements of their simulations if higher grid resolutions and appropriate corresponding physics schemes are used in their studies. Otherwise, some techniques have to be developed (e.g., consuming more convective available potential energy within the convective time scale or diffusing excessive moisture to neighboring points) to remove absolute instability efficiently.

[36] Finally, it is necessary to mention that the initial development of excessive rainfall or NPSs is characterized by rapid increases of the upward motion and low-level converging flows, excessive rainfall, and the progressively upward propagation of grid-box saturation leading to absolute instability, which are all colocated with the center of rapid surface pressure fall. The peak upward motion in EX_36 could reach 3.4 m s^{-1} for A, 1.4 m s^{-1} for B, and 1.2 m s^{-1} for C, with the relative vorticity rapidly increasing to 1–2 × 10^{-4} s^{-1} from the bottom upward (not shown).

Their peak magnitudes and subsequent variations appear to depend highly on the energy supply in the southwesterly flows. Most of the NPSs could maintain their circulations for more than 24 hours, and some for even longer than 48 hours (not shown). After developing sufficient rotation, weaker vertical motions or descending motions may occur near the mesolow center, because converging parcels in the PBL would ascend at some radius from the vortex center as the centrifugal force exceeds the radial pressure gradient force. As a result, more rainfall tends to take place in banded structures at the outer region of the mesolow (e.g., A and B in Figure 7), like typically observed MCSs. Nevertheless, NPSs are often too robust and can produce pronounced modifications to their larger-scale environments and regional climate characteristics.

6. Summary and Conclusions

[37] In this study, sensitivity simulations are performed to examine the impacts of different horizontal resolutions on the simulated summer 1998 extreme rainfall over the YRB-ML region, especially for the heavy rainfall during the second Meiyu rainy phase. It is shown that higher-resolution simulations (e.g., at 4 km) could reproduce reasonably well the rainfall intensity and rainbelt distribution over the YRB-ML during all the Meiyu phases, whereas lower-resolution simulations (e.g., at 36 km) tend to shift the east-west-oriented major rainbelt southwestward and produce more rainfall than that in higher-resolution simulations, and NPSs during the second rainy phase in which vertical (horizontal) wind shears are weak (strong). It appears to be the excessive rainfall that could account for the erroneous southwest-northeast orientation of the Meiyu frontal rainbelt in the lower-resolution simulations.

[38] The excessive rainfall and NPSs are characterized by intense grid-scale precipitation and robust mesolow systems, some of which may be fictitious, stronger low-level southwesterly flows or low-level jets (LLJs), and long periods of cyclonic circulations. In the present case, they tend to be generated during the evening hours when the LLJ is relatively strong, and in the Meiyu frontal zone where convergence of high-θ_e air is high, and aided by the enhanced lifting of high-θ_e air associated with a mesolow to its west. Once generated, they distort the linear cloud and rainfall distribution along the Meiyu front, promote the downstream propagation of pressure perturbations of different scales, and enhance the southward intrusion of cold and dry air from northern China to shift the Meiyu front southwestward, thus producing unrealistic regional climate and weather conditions.

[39] It was found that the simulated excessive rainfall is not evident during the first rainy phase. We attribute this finding to the dominance of significant baroclinic forcing across the Meiyu front with relatively lower-θ_e air in the southwesterly flows. In contrast, the second rainy phase is more thermodynamically driven with much weaker vertical shear but higher across-frontal shear and potential instability over the YRB-ML region. The presence of the high horizontal shear appears to facilitate the development of NPSs as the shear vorticity is transformed to curvature vorticity. The excessive rainfall or NPSs in the lower-resolution simulations can be attributed to CPSs that fail to remove the buildup of potential instability by the warm and moist southwesterly flows and to the slower grid-scale processes in stabilizing the vertical columns. Thus, we may conclude that higher-resolution models with realistic parameterized and grid-scale cloud physics schemes should be adopted to study the regional climate of heavy rainfall events.

References

Bélair, S., and J. Mailhot (2001), Impact of horizontal resolution on the numerical simulation of a midlatitude squall line: Implicit versus explicit condensation, *Mon. Weather Rev.*, *129*, 2362–2376.

Chen, F., and J. Dudhia (2001a), Coupling an advanced land surface-hydrology model with the Penn State-NCAR MM5 modeling system. Part I: Model implementation and sensitivity, *Mon. Weather Rev.*, *129*, 569–585.

Chen, F., and J. Dudhia (2001b), Coupling an advanced land surface-hydrology model with the Penn State-NCAR MM5 modeling system. Part II: Preliminary model validation, *Mon. Weather Rev.*, *129*, 587–604.

Chen, M., and C. Fu (2000), A nest procedure between regional and global climate model and its application in long term climate simulations (in Chinese), *Chin. J. Atmos. Sci.*, *24*, 253–262.

Done, J., C. A. Davis, and M. Weisman (2004), The next generation of NWP: Explicit forecasts of convection using the weather research and forecasting (WRF) model, *Atmos. Sci. Lett. 5*, 110–117.

Dudhia, J. (1989), Numerical study of convection observed during the winter monsoon experiment using a mesoscale two-dimensional model, *J. Atmos. Sci.*, *46*, 3077–3107.

Gao, X., Y. Xu, Z. Zhao, J. S. Pal, and F. Giorgi (2006), Impacts of horizontal resolution and topography on the numerical simulation of East Asian precipitation (in Chinese), *Chin. J. Atmos. Sci.*, *30*, 185–192.

Gao, X., Y. Shi, R. Song, F. Giorgi, Y. Wang, and D. Zhang (2008), Reduction of future monsoon precipitation over China: Comparison between a high resolution RCM simulation and the driving GCM, *Meteorol. Atmos. Phys.*, *100*, 73–86, doi:10.1007/s00703-008-0296-5.

Giorgi, F. (1991), Sensitivity of simulation summertime precipitation over the western United States to different physics parameterizations, *Mon. Weather Rev.*, *119*, 2870–2888.

Giorgi, F., C. Shields Brodeur, and G. T. Bates (1994), Regional climate change scenarios over the United States produced with a nested regional climate model, *J. Clim.*, *7*, 375–399.

Grell, G. A. (1993), Prognostic evaluation of assumptions used by cumulus parameterizations, *Mon. Weather Rev.*, *121*, 764–787.

Hsu, H.-H., Y.-C. Yu, W.-S. Kau, W.-R. Hsu, W.-Y. Sun, and C.-H. Tsou (2004), Simulation of the 1998 East Asian summer monsoon using the Purdue regional model, *J. Meteorol. Soc. Jpn.*, *82*, 1715–1733.

Im, E.-S., E.-H. Park, W.-T. Kwon, and F. Giorgi (2006), Present climate simulations over Korea with a regional climate model using a one way double nested system, *Theor. Appl. Climatol.*, *86*, 187–200.

Janjić, Z. I. (1994), The step-mountain eta coordinate model: Further developments of the convection, viscous sublayer, and turbulence closure schemes, *Mon. Weather Rev.*, *122*, 927–945.

Jha, B., T. N. Krishnamurti, and Z. Christides (2000), A note on horizontal resolution dependence for monsoon rainfall simulations, *Meteorol. Atmos. Phys.*, *74*, 11–17.

Jones, R. G., J. M. Murphy, and M. Noguer (1995), Simulation of climate change over Europe using a nested regional climate model. Part I: Assessment of control climate, including sensitivity to location of lateral boundaries, *Q. J. R. Meteorol. Soc.*, *121*, 1413–1449.

Ju, L. X., and H. J. Wang (2006), Modern climate over East Asia simulated by a regional climate model nested in a global gridpoint general circulation model (in Chinese), *Chin. J. Geophys.*, *49*, 52–60.

Kain, J. S. (2004), The Kain-Fritsch convective parameterization: An update, *J. Appl. Meteorol.*, *43*, 170–181.

Kållberg, P., A. Simmons, S. Uppala, and M. Fuentes (2004), ERA-40 project report series: 17, in *The ERA-40 Archive*, Eur. Cent. for

Medium-Range Weather Forecasts, Reading, U.K., http://www.ecmwf.int/publications/library/do/references/list/192.

Kanamitsu, M., et al. (2002), NCEP-DOE AMIP-II Reanalysis (R-2), *Bull. Am. Meteorol. Soc.*, *83*, 1631–1643.

Kang, I. S. (2007), Integrated climate system modeling in SNU/CES, paper presented at University Allied Workshop, Beijing, 18–20 June 2007.

Kasahara, A. (1961), A numerical experiment on the development of a tropical cyclone, *J. Meteorol.*, *18*, 259–282.

Kieu, C. Q., and D.-L. Zhang (2008), Genesis of tropical storm Eugene (2005) from merging mesovortices associated with ITCZ breakdowns. Part I: Observational and modeling analyses, *J. Atmos. Sci.*, *65*, 3419–3439.

Kitoh, A., and S. Kusunoki (2008), East Asian summer monsoon simulation by a 20-km mesh AGCM, *Clim. Dyn.*, *31*, 389–401, doi:10.1007/s00382-007-0285-2.

Lee, D. K., D. H. Cha, and H. S. Kang (2004), Regional climate simulation of the 1998 summer flood over East Asia, *J. Meteorol. Soc. Jpn.*, *82*, 1735–1753.

Leung, L. R., S. Zhong, Y. Qian, and Y. Liu (2004), Evaluation of regional climate simulations of the 1998 and 1999 East Asian summer monsoon using the GAME/HUBEX observation data, *J. Meteorol. Soc. Jpn.*, *82*, 1695–1713.

Liu, H., D.-L. Zhang, and B. Wang (2008), Daily to submonthly weather and climate characteristics of the summer 1998 extreme rainfall over the Yangtze River Basin, *J. Geophys. Res.*, *113*, D22101, doi:10.1029/2008JD010072.

Lu, L., R. A. Pielke Sr., G. E. Liston, W. J. Parton, D. Ojima, and M. Hartman (2001), Implementation of a two-way interactive atmospheric and ecological model and its application to the central United States, *J. Clim.*, *14*, 900–919.

Mass, C. F., D. Ovens, K. Westrick, and B. A. Colle (2002), Does increasing horizontal resolution produce more skillful forecasts?, *Bull. Am. Meteorol. Soc.*, *82*, 407–430.

Molinari, J., and M. Dudek (1992), Paremeterization of convective precipitation in mesoscale numerical models: A critical review, *Mon. Weather Rev.*, *120*, 326–344.

Petch, J. C., A. R. Brown, and M. E. B. Gray (2002), The impact of horizontal resolution on the simulations of convective development over land, *Q. J. R. Meteorol. Soc. 128*, 2031–2044.

Qian, Y., and F. Giorgi (1999), Interactive coupling of regional climate and sulfate aerosol models over eastern Asia, *J. Geophys. Res.*, *104*, 6477–6499.

Qian, Y., L. R. Leung, S. J. Ghan, and F. Giorgi (2003), Regional climate effects of aerosols over China: Modeling and observation, *Tellus*, *55B*, 914–934.

Reynolds, R. W., and T. M. Smith (1994), Improved global sea surface temperature analyses using optimum interpolation, *J. Clim.*, *7*, 929–948.

Salathé, E. P., Jr., R. Steed, C. F. Mass, and P. H. Zahn (2008), A high-resolution climate model for the U.S. Pacific Northwest: Mesoscale feedbacks and local responses to climate change, *J. Clim.*, *21*, 5708–5726.

Senior, C. A. (1995), The dependence of climate sensitivity on the horizontal resolution of a GCM, *J. Clim.*, *8*, 2860–2880.

Sperber, K. R., S. Hameed, G. L. Potter, and J. S. Boyle (1994), Simulation of northern summer monsoon in the ECMWF model: Sensitivity to horizontal resolution, *Mon. Weather Rev.*, *122*, 2461–2481.

Tang, J., M. Zhao, and B. Su (2006), Effects of model resolution on the simulation of regionally climatic extreme events (in Chinese), *Acta Meteorol. Sinica*, *64*, 432–442.

Wang, W.-C., W. Gong, and H. L. Wei (2000), A regional model simulation of the 1991 severe precipitation event over the Yangtze-Huai River Valley. Part I: Precipitation and circulation statistics, *J. Clim.*, *13*, 74–92.

Wang, Y.-Q., O. L. Sen, and B. Wang (2003), A highly resolved regional climate model (IPRC- RegCM) and its simulation of the 1998 severe precipitation event over China. Part I: Model description and verification of simulation, *J. Clim.*, *16*, 1721–1738.

Xue, Y., R. Vasic, Z. Janjic, F. Mesinger, and K. E. Mitchell (2007), Assessment of dynamic downscaling of the continental U.S. regional climate using the Eta/SSiB regional climate model, *J. Clim.*, *20*, 4172–4193.

Zakey, A. S., F. Giorgi, and X. Bi (2008), Modeling of sea salt in a regional climate model: Fluxes and radiative forcing, *J. Geophys. Res.*, *113*, D14221, doi:10.1029/2007JD009209.

Zhang, D.-L. (1989), The effect of parameterized ice microphysics on the simulation of vortex circulation with a mesoscale hydrostatic model, *Tellus*, *41A*, 132–147.

Zhang, D.-L., H.-R. Chang, N. L. Seaman, T. T. Warner, and J. M. Fritsch (1986), A two-way interactive nesting procedure with variable terrain resolution, *Mon. Weather Rev.*, *114*, 1330–1339.

Zhang, D.-L., E.-Y. Hsie, and M.W. Moncrieff (1988), A comparison of explicit and implicit predictions of convective and stratiform precipitating weather systems with a meso-beta-scale numerical model, *Q. J. R. Meteorol. Soc.*, *114*, 31–60.

Zhang, D.-L., J. S. Kain, J. M. Fritsch, and K. Gao (1994), Comments on: "Parameterization of convective precipitation in mesoscale numerical models: A critical review", *Mon. Weather Rev.*, *122*, 2222–2231.

Zhang, D.-L., W.-Z. Zheng, and Y.-K. Xue (2003), A numerical study of early summer regional climate and weather over LSA-East. Part I: Model implementation and verification, *Mon. Weather Rev.*, *131*, 1895–1909.

H. Liu and B. Wang, LASG, Institute of Atmospheric Physics, Chinese Academy of Sciences, Beijing 100029, China.

D.-L. Zhang, Department of Atmospheric and Oceanic Science, University of Maryland, College Park, MD 20742-2425, USA. (dalin@atmos.umd.edu)